

Graphene-based integrated radiation heat-dissipation reconfigurable polarization conversion metasurface

Bei Dong^{1,§}, Haoran Zu^{1,§}, Rongguo Song^{1,2}(✉), Zhi Luo¹, Wei Qian¹, Ying Huang², Jingwei Zhang¹, Qinglei Du³(✉), Daping He¹

¹ Hubei Engineering Research Center of RF-Microwave Technology and Application, Wuhan University of Technology, Wuhan 430070, China

² Qianyuan National laboratory, Hangzhou 310024, China

³ Air Force Early Warning Academy, Wuhan 430019, China

§ Bei Dong and Haoran Zu contributed equally to this work.

Nano Res., **Just Accepted Manuscript** • <https://doi.org/10.26599/NR.2025.94907494>

<https://www.sciopen.com/journal/1998-0124> on Apr. 21, 2025

© The Authors(s)

Just Accepted

This is a “Just Accepted” manuscript, which has been examined by the peer-review process and has been accepted for publication. A “Just Accepted” manuscript is published online shortly after its acceptance, which is prior to technical editing and formatting and author proofing. Tsinghua University Press (TUP) provides “Just Accepted” as an optional and free service which allows authors to make their results available to the research community as soon as possible after acceptance. After a manuscript has been technically edited and formatted, and the page proofs have been corrected, it will be removed from the “Just Accepted” web site and published officially with volume and article number (e.g., *Nano Research*, **2025**, *18*, 94906990). Please note that technical editing may introduce minor changes to the manuscript text and/or graphics which may affect the content, and all legal disclaimers that apply to the journal pertain. In no event shall TUP be held responsible for errors or consequences arising from the use of any information contained in these “Just Accepted” manuscripts. To cite this manuscript please use its Digital Object Identifier (DOI®), which is identical for all formats of publication.

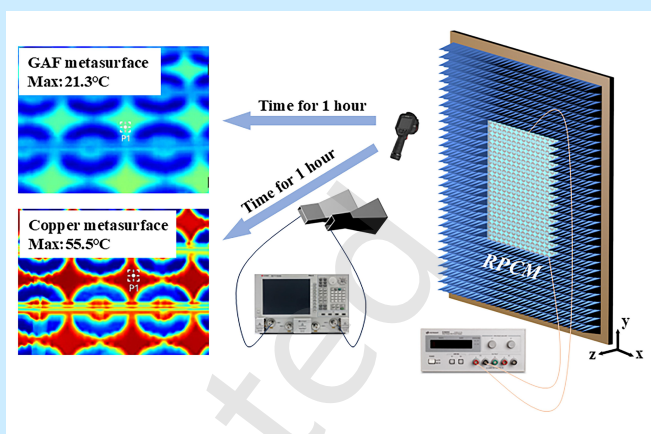
**Graphene-based Integrated Radiation
Heat-Dissipation Reconfigurable Polarization
Conversion Metasurface**

Bei Dong^{1,§}, Haoran Zu^{1,§}, Rongguo Song^{1,2,*}, Zhi Luo¹,
Wei Qian¹, Ying Huang², Jingwei Zhang¹, Qinglei Du^{3,*},
Daping He¹

¹ Wuhan University of Technology, China

² Qianyuan National laboratory, China

³ Air Force Early Warning Academy, China



Graphene-based metasurfaces have the excellent advantage of radiation-heat dissipation multifunctional integration.

Just Accepted

Graphene-based integrated radiation heat-dissipation reconfigurable polarization conversion metasurface

Bei Dong^{1,§}, Haoran Zu^{1,§}, Rongguo Song^{1,2}(✉), Zhi Luo¹, Wei Qian¹, Ying Huang², Jingwei Zhang¹, Qinglei Du³ (✉) and Daping He¹

¹ Hubei Engineering Research Center of RF-Microwave Technology and Application, Wuhan University of Technology, Wuhan 430070, China

² Qianyuan National laboratory, Hangzhou 310024, China

³ Air Force Early Warning Academy, Wuhan 430019, China

[§] Bei Dong and Haoran Zu contributed equally to this work.

© The Author(s) 2025

Received: 27 March 2025 / Revised: 19 April 2025 / Accepted: 21 April 2025

ABSTRACT

In active reconfigurable polarization conversion metasurfaces, the integration of electromagnetic radiation performance and heat dissipation efficiency presents two critical challenges. In this work, we proposed a graphene-based reconfigurable polarization metasurface that integrates heat dissipation and electromagnetic regulation functions. The proposed graphene metasurface modulates the polarization state of the reflected wave at multiple frequency bands via the on-off switching of PIN diodes. When the PIN diode is in the ON state, the metasurface can modulate the incident linear polarization wave into its cross-polarization wave in 5.73 - 6.15 GHz and 11.25 - 13.1 GHz, and into a circular polarization wave in 6.27 - 10.18 GHz. When the PIN diode is switched to the off state, the cross-polarization transitions are achieved in 5.75 - 7.32 GHz and 12.83 - 14.24 GHz, with full reflection in the band of 7.92 - 10.15 GHz, and circular polarization in 12.83 - 14.24 GHz. In addition, when the graphene metasurface system worked after a long period of operation, the temperature of the graphene metasurface is 21.3 °C, which is 34.2 °C lower than that of the copper metasurface, this has less impact on the temperature drift effect of the PIN diode. The integrated graphene polarized reconfigurable metasurface for radiation and heat dissipation addresses the performance, volume, and thermal management limitations of traditional systems through multifunctional integration and dynamic tunability, offering significant potential for future smart electromagnetic devices application in communication, radar, and Internet of Things.

KEYWORDS

graphene film, reconfigurable polarization conversion metasurface, graphene metasurface, integrated radiation heat dissipation

1 Introduction

With the rapid development of wireless communication, radar detection and satellite navigation, the demand for dynamic regulation of electromagnetic wavefront is increasingly urgent. As an emerging artificial electromagnetic metasurface, reconfigurable polarization conversion metasurface (RPCM) is capable of realizing dynamic switching of reflected wave polarization state by real-time modulation of the equivalent electromagnetic parameters of the unit structure [1, 2], which provides a revolutionary solution to break through the functional limitations of traditional metasurfaces. However, with the extension of the operating frequency to the millimeter wave band [3, 4] and the continuous increase of the system power density, such devices face two mutually constraining challenges. Firstly, under dense integration and high-power operation, the thermal accumulation effect triggered by the Joule loss and conductor

loss of the semiconductor devices leads to the performance degradation such as resonance frequency shift [5] and the decrease of the polarization conversion efficiency [6]. In addition, the traditional separated heat dissipation design leads to the system volume [7, 8], the traditional separated heat dissipation design leads to the expansion of system volume, which is in fundamental contradiction with the sub-wavelength cell size required for the metasurface [9]. This “thermal-electrical-structural” multi-physical field coupling problem has become a key bottleneck in restricting highly reliable active metasurfaces [10, 11].

Currently, two types of technology routes are mainly used to address these challenges. One approach is to optimize the semiconductor device to reduce the conduction loss [12, 13], however, this method has the challenges of high material cost and complex processing [14, 15]. The other approach is based on the microfluidic embedded substrate passive heat

dissipation scheme [16, 17], however, this type of design introduces additional RF signal attenuation and restricts the density of the cell row [18, 19]. It is worth noting that in recent years, the materials science breakthroughs for this problem provides a new solution to the graphene film [20-22] because of its compatibility with ultra-high electrical conductivity (1.59×10^6 S/m) and thermal conductivity (1400.3 W / (m · K) [23, 24], which lays a physical foundation for its application in multi-functional integrated electromagnetic devices [25, 26].

Graphene possesses extremely excellent thermal, electrical, and mechanical properties [20-22]. In an ideal state, graphene is globally recognized as a material with high thermal conductivity, lightweight texture [27, 28], and environmental friendliness [21], and its electrical conductivity is even comparable to that of metals [23, 24]. Currently, some researchers have already applied graphene-based heat dissipation materials in practice. For example, in reference [29], a heat-dissipating mobile antenna was proposed. By using novel graphene with high electrical conductivity to design the antenna, its high thermal conductivity also facilitates heat dissipation [30, 31], achieving the sharing of materials and space between the antenna and heat dissipation, and greatly expanding the space for both. The experimental data shows that, compared with the traditional heat dissipation design, after adopting this scheme, the maximum temperatures of the heat sources of the system-on-chip and the camera have both decreased significantly. This concept can simultaneously reduce the requirement for antenna clearance and cool down the terminal without any compromise, thereby strongly confirming the powerful substitutability of graphene materials in the field of electromagnetic-thermal synergy.

This paper proposes a RPCM, aiming to address the thermal accumulation effect caused by multi-device integration. This effect exacerbates the temperature drift of the PIN diode [32, 33], which in turn leads to problems such as frequency shift and decline in polarization conversion efficiency [34, 35]. The RPCM uses graphene materials with high thermal conductivity and high electrical conductivity to replace the traditional metal material, copper, providing an ideal carrier material for high-density integrated electronic systems. In the designed structure, graphene is used for the top layer structure of the metamaterial and the ground plane that reflects electromagnetic waves, effectively dissipating the heat generated by active devices. The proposed RPCM realizes the conversion from linear polarization (LP) to cross polarization (CRP), from LP to left-hand circular polarization (LHCP), and from LP to full reflection co-polarization (COP) in seven different frequency bands by adjusting the state of the embedded PIN diodes. When the PIN diodes are in the ON state, the metasurface can not only achieve CRP conversion in lower and higher frequency bands but also realize the conversion from LP to LHCP in the middle frequency band. When the PIN diodes are in the OFF state, the metasurface realizes the conversion from LP to CRP, COP, and LHCP in other frequency bands. In addition, in order to verify that the graphene based RPCM has a stronger heat dissipation capability than the copper based RPCM under high-power and long-term working conditions [36, 37], we tested the maximum temperatures on the surface of the RPCM at the initial working stage and the

long-term working stage when the PIN diode is in the on or off state. The results show that the surface temperature of the graphene based RPCM under long term steady state operation is 21.3 °C, while that of the copper based RPCM is 55.5 °C. The former is 34.2 °C lower than the latter, fully demonstrating the excellent heat dissipation performance of high thermal conductivity graphene materials.

2 Experimental

2.1 Fabrication of Graphene Film

The fabrication of highly thermally conductive and electrically conductive graphene film involves a multistep process combining high-temperature graphitization and mechanical densification [23]. Initially, a graphene oxide (GO) suspension (15 mg/mL) is uniformly deposited onto a flexible polyethylene terephthalate (PET) substrate through blade-coating, followed by low-temperature drying at 70 – 80 °C to form a uniform precursor film. To achieve enhanced crystallinity and conductivity, the GO film undergoes a two-stage ultrahigh-temperature annealing protocol: first at 1300 °C for 2 hours under argon atmosphere to remove oxygen functional groups, followed by a critical graphitization step at 2850 °C for 1 hour to reconstruct the sp^2 carbon network. Subsequent mechanical consolidation via high-pressure rolling (200 MPa) eliminates interlayer voids. Finally, the graphene film undergoes re-annealing at 2850 °C and high-pressure rolling (200 MPa) to further to optimize the interlayer stacking order.

2.2 Fabrication of RPCM

The laser engraver (LPKF Protolaser U4) is employed to pattern graphene films, adjusting the laserpower and scanning speed to ensure optimal depth of cut and edge quality of the graphene metasurface unit and the unwanted parts are delicately removed. Subsequently, we use a spray coating technique to uniformly apply an aerosol layer onto the F4B surface. We then laminated the pre-peeled graphene pattern onto the F4B surface, removing any air bubbles through roller pressing. Finally, the sample was heated to cure the aerosol. Then, the heating process enabled the successful transfer of the graphene pattern to the F4B substrate. Finally, a silver glue (double bonding chemical DB2013) is used to form a robust and effective electrical connection by sequentially connecting the PIN diode (SMP1320-040LF) to the bias linear positive and negative terminals of the designed metasurface top structure.

3 Results and discussion

3.1 Characterization of Graphene Film

Figure 1(a) shows the digital photo of graphene film with physical size of 50 cm × 50 cm. In addition, the illustration in Figure 1(a) illustrates that graphene film has excellent thermal conductivity properties. Graphene film exhibits anisotropic structures, characterized by a dense, continuous layered morphology in the cross-sectional direction, as illustrated in Figures 1(b) and 1(c). The high-temperature reduction process, which involves the removal of oxygen-containing functional groups and the rearrangement of carbon atoms, results in the formation of surface wrinkles (Figure 1(d)). These wrinkles facilitate the ability of graphene film to fully recover its original structure and properties after repeated deformation, thereby enhancing the mechanical flexibility of graphene films. As

illustrated in Figures 1(e) and 1(f), the white light interference microscopy reveals a surface roughness of $0.65 \mu\text{m}$ for the graphene film. In the Raman spectrum, the D peak at 1347 cm^{-1} is nearly absent and the ID/IG ratio is 0.0024, suggesting that the precursor defects have been effectively repaired and a graphitized structure has been achieved (Figure 1(g)). The X-ray diffraction (XRD) pattern exhibits sharp diffraction peaks (002) centered at approximately 26.5° , indicating that the graphene film has a stacking of graphene layers and with an interlayer spacing of $\sim 0.34 \text{ nm}$. In addition, the diffraction peak

(004) indicates the graphene film has a high degree of graphitization (Figure 1(h)). High-resolution transmission electron microscopy (HRTEM) image reveals that the lattice spacing of the graphene film along the 002 direction is 0.34 nm (Figure 1(i)), consistent with the theoretically predicted graphite interlayer spacing. The characterization results indicate that the graphene films exhibit a high degree of graphitization and excellent crystallinity, both of which facilitate efficient electron and phonon transport.

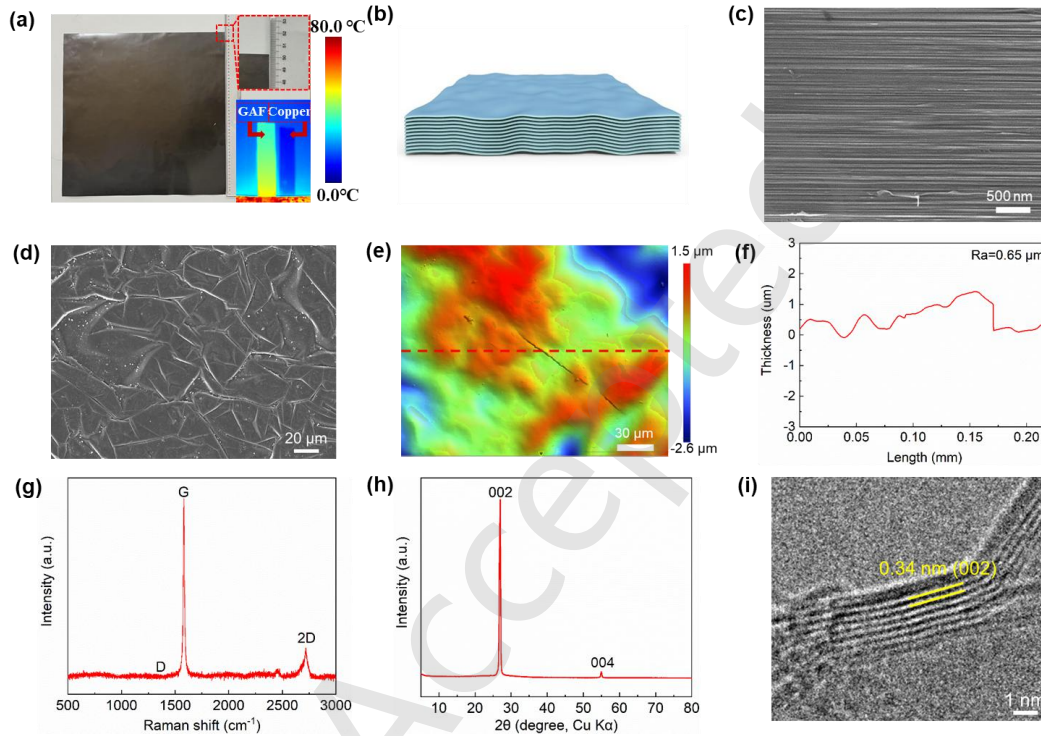


Figure 1 Structural Characterization of graphene film. (a) Digital photograph of graphene film and measured thermal results when using copper foil and graphene film. (b) Schematic diagram of the structural model of the graphene film. (c) Cross-section SEM image of graphene film. (d) Surface SEM image of graphene film. (e, f) Surface morphology and roughness analysis of graphene film. Raman spectrum (g), XRD pattern (h), and HRTEM image (i) of graphene film.

3.2 Design and working principles of RPCM

The proposed structure is a reflective reconfigurable polarization conversion metasurface with polarization conversion functionalities as illustrated in Figure 2(a). When the PIN diodes are forward-biased (as shown in Figure 2(a)), the incident linear polarization wave oriented at $\varphi+90^\circ$ ($\varphi=45^\circ$) relative to the x-axis undergoes distinct polarization transformations across three operational bands, and Figure S(1) shows the reflection coefficient and phase difference in this case. CRP reflected wave dominates in the 5.73 - 6.15 GHz and 11.25 - 13.1 GHz frequency ranges, while efficient conversion to LHCP reflection occurs between 6.27 - 10.18 GHz. Under reverse-biased PIN diode conditions, the RPCM exhibits enhanced diversity of polarization mode across four frequency bands, while Figure S(2) simulates the reflection coefficient and the phase difference. CRP reflected wave is achieved in dual bands spanning 5.75 - 7.32 GHz and 12.83 - 14.24 GHz. Notably, full reflective COP is maintained in 7.92 - 10.15 GHz, while a LHCP conversion band emerges between 11.5 GHz and 12.14 GHz. This three-state reconfiguration capability enables

dynamic polarization manipulation through bias control, demonstrating broadband performance with multiple functional bands in both linear and circular polarization domains. The frequency dependent polarization transitions are achieved through the integration of PIN diodes that modulate the electromagnetic response of the RPCM. The operational bandwidths and polarization conversion ratios are optimized through geometric parameter engineering of the unit cells, ensuring stable phase gradient control across specified frequency ranges during state switching.

As illustrated in Figure 2(b) and 2(c), the proposed RPCM unit cell consists of three fundamental components: a top patterned layer, a ground plane, and a dielectric substrate. The top layer features periodically arranged butterfly-shaped patches loaded with PIN diodes, whose distinctive dual-wing geometry is oriented along the $\pm 45^\circ$ directions relative to the x-axis to enable polarization manipulation. Two dedicated DC bias linear are integrated on the top layer to provide precise voltage control for the PIN diodes, ensuring stable switching characteristics. The substrate is composed of low-loss F4B with

a height of h , a relative permittivity of $\epsilon_r = 2.2$ and loss tangent $\tan\delta = 0.0015$, selected for its excellent high-frequency stability. Both the top radiating structure and bottom ground plane are fabricated using graphene film. Embedded in the center of the top structure is a PIN diode, which can be equated to an RLC series circuit, which is equivalent to a series connection of resistor R_{off} and capacitor C_{off} in the closed state of the PIN

diode, and a series connection of resistor R_{on} and inductor L_{on} in the open state of the PIN diode, lumped elements are $R_{off} = 6.12\text{ohm}$, $C_{off} = 0.22\text{pF}$, $R_{on} = 2.2\text{ohm}$, $L_{on} = 0.25\text{nH}$. The software CST 2021 is used to simulate and analyze the RPCM using Floquet port and periodic boundary conditions. The optimized unit structure parameters are given in Table 1.

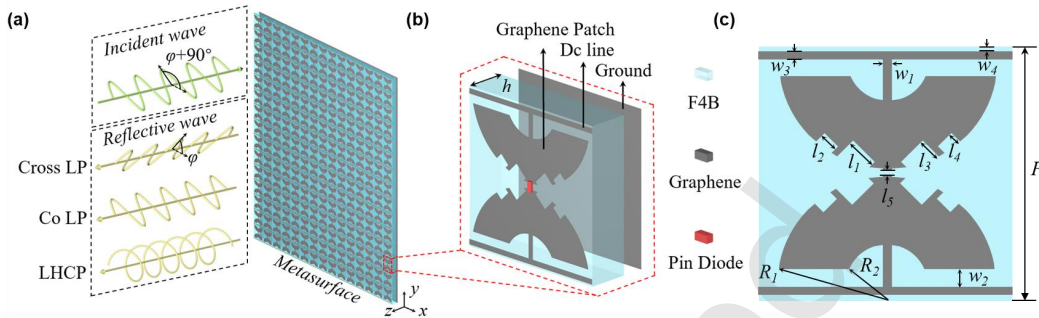


Figure 2 Structural schematic of the proposed RPCM. (a) Functional diagram. (b) RPCM unit cell structure. (c) Top view of unit cell.

Table 1 Parameters of the proposed RPCM

Parameters	l_1	l_2	l_3	l_4	l_5	R_1	R_2
Values (mm)	1.6	1.2	1.28	0.8	1.8	7.2	3
Parameters	w_1	w_2	w_3	w_4	h	P	
Values (mm)	0.5	0.8	0.5	0.4	4	15	

In order to explain the working principle of RPCM, the mechanism can be clarified by the current distribution of the incident wave excitation. The current density distributions during PIN diode turn off at resonant frequencies 6, 8.57 and 13.54 GHz are shown in Figure 3. According to Figure 3(a), an incident LP wave at an angle of -45° along the x-axis can be

decomposed into the u-axis or the v-axis. To verify this characteristic, we simulated the reflection amplitude and phase difference in the uv coordinate system, and the simulation results are shown in Figures S(3) and S(4), which indicates that within the operating frequency range, $|R_{uu}|$ and $|R_{vv}|$ are almost equal to 1, which fully demonstrates that the RPCM has the characteristic of a low loss factor. In addition, the CRP conversion frequency bands are marked in gray, while the phase difference between the reflected waves in the u and v directions is close to $\pm 180^\circ$, achieving perfect cross-polarization conversion. The LHCP is marked in pink. When the phase difference between the u and v directions is close to -90° , a well performing LHCP reflected wave is obtained. The COP conversion bands are marked in blue. At this time, the phase difference between the u and v directions is neither close to $\pm 90^\circ$ nor $\pm 180^\circ$, so the incident wave is totally reflected.

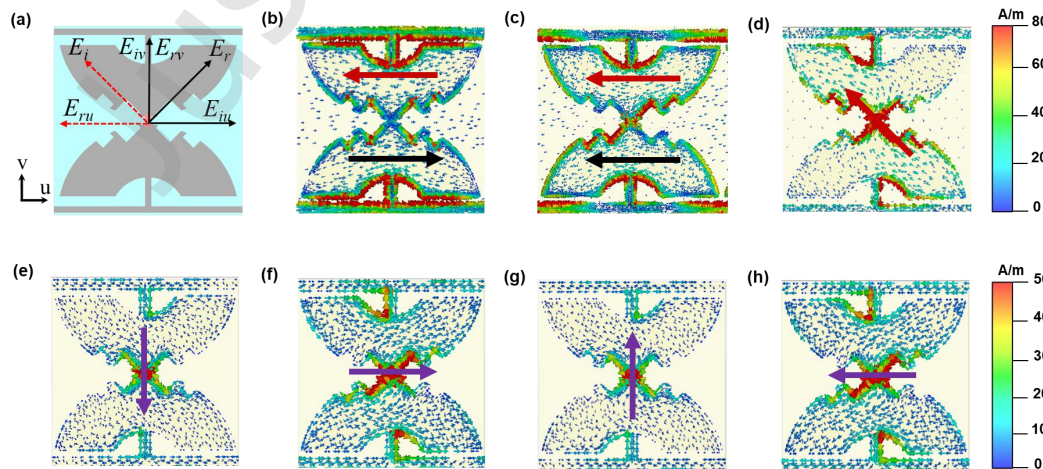


Figure 3 (a) Schematic of the decomposition of the incident and reflected electric fields. (b)-(d), The surface current density distributions of the top and bottom layers at (b) 6GHz, (c) 13.54GHz and (d) 8.57GHz for an incident linear polarization wave oriented at $\varphi + 90^\circ$ ($\varphi = 45^\circ$) relative to the x-axis. (e)-(h) The induced currents in the top layer at 9 GHz corresponding to the different phases are distributed as (e) 0° , (f) 90° , (g) 180° and (h) 270° .

In the u-axis, as shown in Figure 3(b), at 6 GHz, the currents on the top (red arrows) and bottom (black arrows) are

reversed and parallel, and then a magnetic dipole resonance is formed along the v -direction. As a result, the equivalent permeability of the electric field in the v -direction is significantly larger, leading to a higher impedance surface and an inconsistent phase of the reflected electric field along the v -direction. However, in the u -direction, there is no dipole resonance and the reflected electric field is in phase with the incident electric field. Because of this, the synthesized reflected field is at an angle of $+45^\circ$ along the x -axis at 6 GHz. As shown in Figure 3(c), the currents in the top and bottom layers at 13.54 GHz induce parallel in-phase currents in the u -direction, forming an electric dipole resonance. Then, the equivalent dielectric constant of the electric field in the corresponding direction is large, resulting in a low impedance surface. This means that the reflected wave is in phase with the incident wave. Since the electric field radiated by the electric dipole is in phase with respect to the dipole moment, the reflected wave along the dipole direction is also in phase as in the case of the magnetic dipole resonance. Thus, the CRP transition is also achieved. As shown in Figure 3(d), the surface current of the upper mechanism at 13.54 GHz is at an angle of -45° along the x -axis, and the direction of the electric field radiated by it is in the same direction as the current oscillation direction, so the polarization of the reflected wave remains at the angle of -45° along the x -axis. For the linear to circular polarization transition of the loaded PIN diode, the current distributions in the top layer at different excitation phases at a resonant frequency of 9 GHz are shown in Fig. 3e-h. The purple arrow represents the direction of the induced current in the top layer. As the phase of the incident electric field varies from 0° to 270° , the surface current rotates in the counterclockwise direction, verifying that the reflected wave is an LHCP wave.

3.3 Measurement results and analysis

The multi-frequency RPCM measurement system is shown in Figure 4(a). The whole system includes a Vector Network

Analyzer (VNA) and a microwave darkroom. We fabricated and measured a 15×15 prototype based on the RPCM structural unit in Figure 2(b), and the experimental structures and fabricated prototypes for graphene metasurfaces and copper metasurfaces are shown in Figure 4(b-e), with a fabricated sample period of 225 mm. The RPCM to be tested was fixed in the center of the platform with an absorber, and was secured with non-conductive tape to minimize parasitic coupling. The platform was placed at a distance of 2 m from the EM wave transmitting antenna to ensure that the far-field test requirements could be achieved, and the receiving antenna was placed next to the transmitting antenna. The RPCM was placed at the mid-pituitary line in the horizontal direction of the transmitting and receiving antennas, which ensured that the angle of the incident wave and the reflected wave was not more than 5° , reducing the measurement error. Both the transmitting and receiving antennas are connected to the vector network analyzer with coaxial cables, and their reflection coefficients can be measured after calibration, and measure the data of the copper plate for calibration (as shown in figure S(5)). Free space measurements were used for the measures and a time domain gate was added to filter out the clutter.

All simulation and measurement results are shown in Figure 4(f-i). The black realization indicates the simulation results, the pink line indicates the base graphene RPCM measured results, and the blue dashed line indicates the base copper RPCM measured results. The gray shaded area represents the linear-to-cross-polarization conversion band and the linear-to-left-handed circular polarization conversion band, while the pink shaded area represents the co-polarization total reflection band. The measured and simulated results of RPCM fabricated by graphene and copper are in good agreement in the frequency bands with polarization conversion ratio (PCR) $> 90\%$ and axial ratio (AR) < 3 dB, indicating that graphene can be used as an alternative to copper for fabricating the metasurfaces in terms of electromagnetic properties.

Table 2 Comparison with previous RPCM

Ref.	PIN State	Incident Pol.	Output Pol.	Bands (GHz)	PCR	Cell size(mm ³)
[38]	ON	LP	LP	3.83-4.74	/	24.5×24.5×5.1
	OFF	LP	Cross LP	3.39-5.01	88%	
[39]	ON	LP	Cross LP	10.5-13.9/17.7-27.2	90%	8×8×2
	OFF	LP	CP	11.8-24.1	/	
[40]	ON	LP	LP	7.4-12	/	17×17×2.9
	ON	CP	Cross CP	8-12	80%	
	OFF	LP	Cross LP	7.4-12	/	
	OFF	CP	CP	8-12	/	
[41]	ON	LP	Cross LP	3.77-6.2	90%	15×15×5.6
	ON	LP	LHCP	7.75-8.6	/	
	OFF	LP	RHCP	5.2-6.1	/	
	OFF	LP	LP	2-3.66/8.42-9.52	/	

This work	ON	LP	Cross LP	5.73-6.15/11.25-13.1	90%	15×15×4
	ON	LP	LHCP	6.27-10.18	/	
	OFF	LP	Cross LP	5.75-7.32/12.83-14.24	90%	
	OFF	LP	LHCP	11.5-12.14	/	
	OFF	LP	Co LP	7.92-10.15	90%	

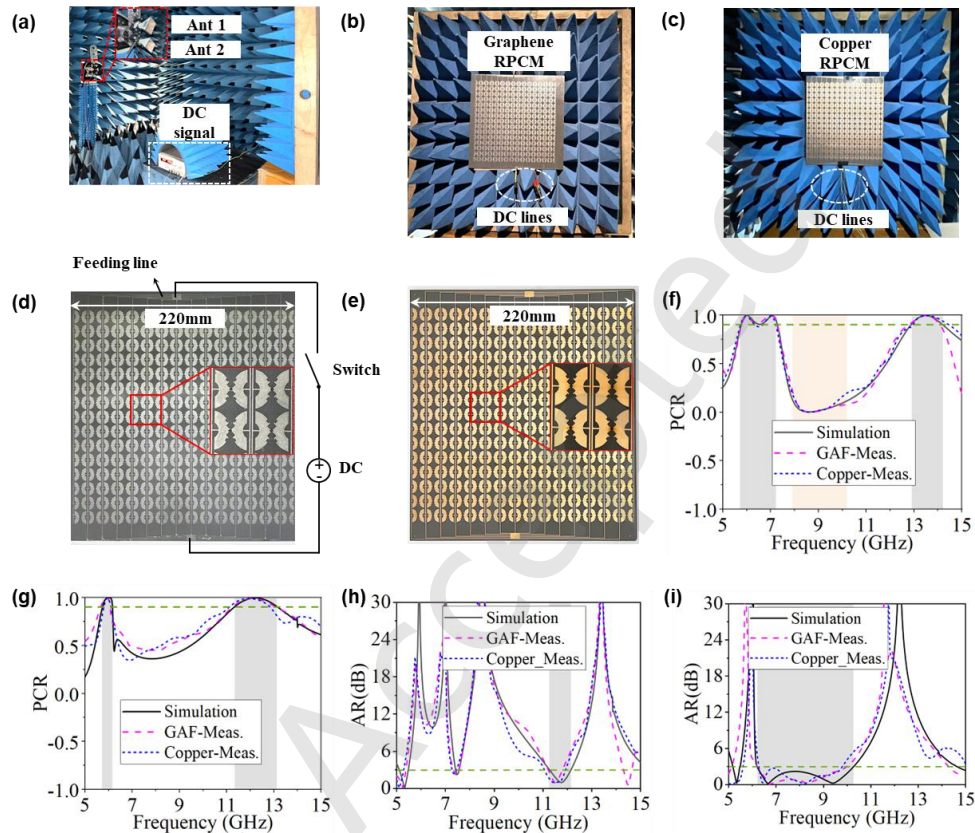


Figure 4 Performance of the proposed RPCM. (a) Multiband reconfigurable polarization metasurface measurement system. (b) experimental configuration of the graphene metasurface. (c) experimental configuration of the copper metasurface. (d) photograph of the graphene metasurface prototype. (e) photograph of the copper metasurface prototype. Comparison of experimental and simulation results: (f) PCR, PIN off. (g) PCR, PIN on. (h) AR, PIN off. (i) AR, PIN on.

To demonstrate the good performance of the proposed RPCM, Table 2 compares the functionality of the proposed metasurfaces with the state-of-the-art features, including operating modes and frequency bands. All the designs are reflective active metasurfaces controlled by the state of the PIN diode. As can be seen from the table, the designed metasurface antenna not only achieves a polarization conversion efficiency of more than 90% for multi-frequency multimode reconfigurable polarization the operating band, but also has a low profile of $0.08 \lambda_0$.

3.4 Investigation of thermal performance of graphene and copper RPCM

The core of the proposed RPCM to dynamically regulate the electromagnetic wave polarization state through the on or off state of PIN diodes. This active device consumes power when it is forward biased and carries RF signals at the same time, and its internal resistance converts part of the input power into heat. Meanwhile, the PIN diodes generates dynamic losses

when switching on and off, which also leads to an increase in its temperature. When the metasurface integrated with multiple active devices is in a high-power operating state, the energy loss of each unit increases, leading to a local temperature increase, which affects the temperature drift of the PIN diode due to its temperature sensitivity, resulting in changes in the PIN diode equivalent resistance inductance and capacitance, which leads to a weakening of the polarization conversion efficiency of the metasurface, as well as a shift in the resonance frequency.

In order to demonstrate that graphene-based metasurfaces have good integrated electromagnetic radiation and heat dissipation capabilities, the copper-based and graphene-based metasurfaces are investigated here under a 5 V positive feed constant voltage provided by a DC regulated power supply, model KEYSIGHT B2901, and observed using an infrared camera, model HM-TP76-25SVFW. This thermal imaging camera has 640×512 pixels and has a temperature test range of

-20° to 650° with an accuracy of 2%. During the test, the thermal imaging camera was kept parallel to the metasurface and at a distance of 25 mm from it. The thermal imaging camera displayed the temperature distribution as well as the center temperature of the image. The cross-PCR and AR of both were also tested by VNA for long time operation.

Figures 5(a-d) show the surface temperatures of the RPCM made of copper and graphene at the initial time of operation and at an operation time of $t = 1$ h. From Figs. 5a and 5b, it can be seen that the surface temperatures of the copper fabricated RPCM and graphene fabricated RPCM are lower at the initial working time, which are both around 12.9 °C, and the PIN diodes do not show any significant temperature drift effect. While Fig. 5c and Fig. 5d show that the surface temperature of the graphene super-surface is 21.3 °C when the power is continuously turned on for 1 h, the surface temperature of the RPCM made of copper reaches 55.5 °C, which is 34.2 °C higher than that of the RPCM made of graphene, indicating that the RPCM made of graphene, has a superior heat dissipation ability, and the Joule heat generated by the PIN diode can be dissipated through the graphene material. Joule heat energy generated by

the PIN diode is better transmitted to the surrounding environment through the graphene structure.

Figure 5(e-h) shows the PCR and AR of the copper RPCM and graphene RPCM in the PIN-off and PIN-on states measured by the VNA during 1 h. It can be clearly observed that the copper RPCM has a narrower frequency band and resonance frequency shift in the PIN-off state, and the low-frequency polarization conversion efficiency decreases to below 80%, the PCR >90% bandwidth gets narrower of high frequency bands in the PIN-on state. The polarization conversion efficiency in the low-frequency band decreases to below 80% in the open state of the PIN diode, the operating bandwidth of more than 90% of the PCR in the high-frequency band has been narrowed, the bandwidth of the AR<3 dB decreases, and the undesired operating band appears in the high frequency. The measured PCR and AR of RPCM made of graphene in both on and off state of PIN diodes fit the simulation curves, which proves that the temperature drift effect of heat dissipation PIN diode is lower when it works for a long time, and the influence on the electromagnetic performance of the RPCM is lower.

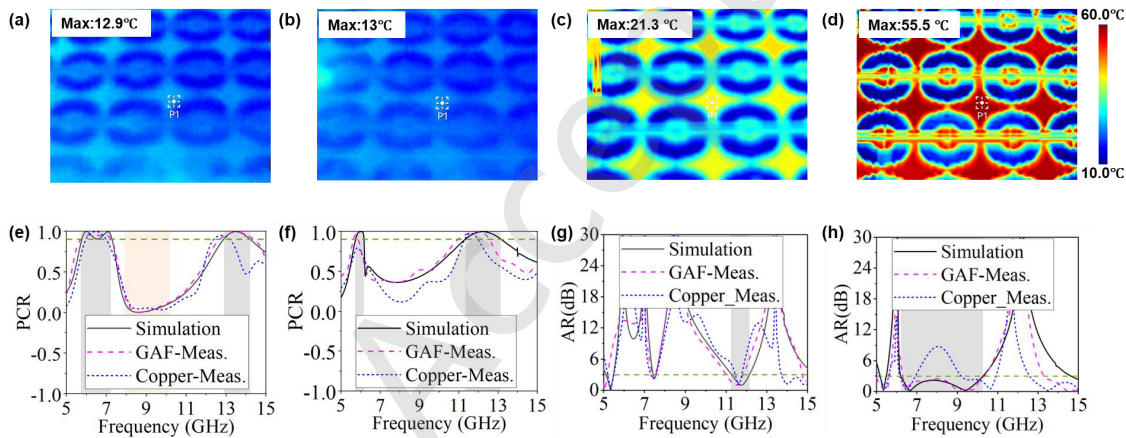


Figure 5 Comparison of the thermal performance of graphene metasurface and copper metasurface initially and after 1h of applied voltage of 5 V. (a) Infrared imaging of graphene metasurface under short-time applied voltage. (b) Infrared imaging of copper metasurface under short-time applied voltage. (c) Infrared imaging of graphene metasurface under long-time applied voltage. (d) Infrared imaging of copper metasurface under long-time applied voltage. Polarization conversion performance of RPCM after applying voltage to the PIN diode for 1 h. (e) Comparison of PCR simulation of PIN diode in closed state with actual measurement. (f) Comparison of PCR simulation of PIN diode in open state with actual measurement. (g) Comparison of AR simulation of PIN tube in closed state with actual measurement. (h) Comparison between AR simulation and real test in the open state of the PIN diode.

4 Conclusions

In conclusion, this work proposes a radiation-heat-integrated reconfigurable polarization conversion metasurface based on high thermal conductivity and high conductive graphene film. The excellent heat dissipation capability of graphene film provides a stable working environment for the electromagnetic performance of the PIN diode modulated metasurface. When the embedded PIN diodes are in the ON state, the incident LP incident wave will be converted into CRP reflected wave in 5.73 - 6.15 GHz and 11.25 - 13.1 GHz, and LHCP in the 6.27 - 10.18 GHz band. If the PIN diodes are turned off, CRP conversion occurs in the 5.75 - 7.32 GHz and 12.83 - 14.24 GHz, COP is achieved in 7.92 - 10.15 GHz, and the conversion from LP to LHCP is obtained in the 12.83 - 14.24 GHz. The experimental results are in good

agreement with the simulation results. In addition, the heat dissipation experiments based on graphene and copper metasurfaces further demonstrate that the graphene film with high thermal conductivity will diffuse the heat generated from the PIN diode operation as well as the radiation of the top structure to the surroundings faster, which contributes to avoiding the temperature drift effect of the PIN diodes, and ensures the stability of the system. This integrated design concept applies not only to reconfigurable polarization conversion metasurfaces but also to beam scanning antennas, stealth suits, etc. It offers a new path for 6G, quantum radar, and radar detection, enhancing communication system design and promoting multifunctional integrated devices from lab to engineering.

Acknowledgements

This work was supported by the National Natural Science Foundation of China (51672204) and Hubei Provincial Natural Science Foundation of China (2025AFB082).

References

- [1] Yu, N.; Capasso, F. Flat optics with designer metasurfaces. *Nat. Mater.* **2014**, *13*, 139–150.
- [2] Glybovski, S. B.; Tretyakov, S. A.; Belov, P. A.; Kivshar, Y. S.; Simovski, C. R. Metasurfaces: From microwaves to visible. *Phys. Rep.* **2016**, *634*, 1–72.
- [3] Gu, X.; Liu, D.; Sadhu, B. Packaging and Antenna Integration for Silicon-Based Millimeter-Wave Phased Arrays: 5G and Beyond. *IEEE J. Microw.* **2021**, *1*, 123–134.
- [4] Hashemi, H. Millimeter-wave power amplifiers & transmitters. *CICC 2017*. **2017**, 1–8.
- [5] Liu, B.; Liu, J.; Hu, C. C.; Song, K. X.; Huang, Y. H. Low-temperature co-fired ceramics with high thermal expansion and reliability for millimeter-wave antennas. *Cell Rep. Phys. Sci.* **2024**, *5*, 101959.
- [6] Lu, T. J.; Jin, J. M. Electrical-Thermal Co-Simulation for Analysis of High-Power RF/Microwave Components. *IEEE Trans. Electromagn. Compat.* **2017**, *59*, 93–102.
- [7] Bar-Cohen, A.; Wang, P. Thermal Management of On-Chip Hot Spot. *ASME*. **2012**, *134*, 051017.
- [8] Garimella, S. V.; Fleischer, A. S.; Murthy, J. Y.; Keshavarzi, A.; Prasher, R.; Pate, C. Thermal Challenges in Next-Generation Electronic Systems. *IEEE Trans. Compon. Packag. Technol.* **2008**, *31*, 801–815.
- [9] West, P. R.; Stewart, J. L.; Kildishev, A. V.; Shalaev, V. M.; Shkunov, V. V.; Strohkendl, F.; Zakharenkov, Y. A.; Dodds, R. K.; Byren, R. All-dielectric subwavelength metasurface focusing lens. *Opt. Express.* **2014**, *22*, 26212–26221.
- [10] Zhang, H. H.; Liu, X. Y.; Liu, Y.; Fan, Z. C.; Du, H. L. Thermal-Mechanical-Electromagnetic Multiphysics Simulation of Satellite Phased Array Antenna Based on DGTd and FEM Method. *IEEE J-MMCT*. **2024**, *9*, 236–246.
- [11] Zheng, W.; Jia, X. Y.; Zhou, Z. Y.; Yang, J.; Wang, Q. W. Multi-physical field coupling simulation and thermal design of 10 kV-KYN28A high-current switchgear. *Therm. Sci. Eng. Prog.* **2023**, *43*, 101954.
- [12] Shahil, K. M. F.; Balandin, A. A. Thermal properties of graphene and multilayer graphene: Applications in thermal interface materials. *Solid State Commun.* **2012**, *152*, 1331–1340.
- [13] Moore, A. L.; Shi, L. Emerging challenges and materials for thermal management of electronics. *Mater Today*. **2014**, *17*, 163–174.
- [14] McCluskey, P. Reliability of Power Electronics Under Thermal Loading. *2012 7th CIPS*. **2012**, 1–8.
- [15] Shnawah, D. A.; Sabri, M. F. M.; Badruddin, I. A. A review on thermal cycling and drop impact reliability of SAC solder joint in portable electronic products. *Microelectron Reliab.* **2012**, *52*, 90–99.
- [16] Hajmohammadi, M. R.; Alipour, P.; Parsa, H. Microfluidic effects on the heat transfer enhancement and optimal design of microchannels heat sinks. *Int. J. Heat Mass Transfer*. **2018**, *126*, 808–815.
- [17] Kandlikar, S. G.; Grande, W. J. Evolution of Microchannel Flow Passages--Thermohydraulic Performance and Fabrication Technology. *Heat Transfer Eng.* **2003**, *24*, 3–17.
- [18] Xu, C.; Ren, Z. H.; Wei, J. X.; Lee, C. K. Reconfigurable terahertz metamaterials: From fundamental principles to advanced 6G applications. *iScience*. **2022**, *25*, 103799.
- [19] Jiang, B.; Hu, H.; Tian, J.; Lei, S.; Wu, Y.; Chen, B. An Active Multifunctional Metamaterial With Four Operating Modes. *IEEE Trans. Antennas Propag.* **2024**, *72*, 4221–4231.
- [20] Novoselov, K. S.; Geim, A. K.; Morozov, S. V.; Jiang, D.; Zhang, Y.; Dubonos, S. V.; Grigorieva, I. V.; Firsov, A. A. Electric Field Effect in Atomically Thin Carbon Films. *Science*. **2004**, *306*, 666–669.
- [21] Geim, A.; Novoselov, K. The rise of graphene. *Nat. Mater.* **2007**, *6*, 183–191.
- [22] Balandin, A. A.; Ghosh, S.; Bao, W. Z.; Calizo, I.; Teweldebrhan, T.; Miao, F.; Lau, C. N. Superior Thermal Conductivity of Single-Layer Graphene. *Nano Lett.* **2008**, *8*, 902–907.
- [23] Song R. G.; Jiang S. Q.; Hu Z.L.; Fan C.; Li P.; Ge Q.; Mao B. Y.; He D. P. Ultra-high conductive graphene assembled film for millimeter wave electromagnetic protection. *Sci. Bull.* **2022**.
- [24] Li L., Yang J. L., et al. Large-scale current collectors for regulating heat transfer and enhancing battery safety. *Nat. Chem. Eng* **2024**, *1*, 542–551.
- [25] Zeng, B.; Huang, Z.; Singh, A. Hybrid graphene metasurfaces for high-speed mid-infrared light modulation and single-pixel imaging. *Light Sci Appl.* **2018**, *7*, 51.
- [26] Sun, S.; Jiao, D. Multiphysics Modeling and Simulation of 3-D Cu–Graphene Hybrid Nanointerconnects. *IEEE T-MTT* **2020**, *68*, 490–500.
- [27] Kim, K. S.; Zhao, Y.; Jang, H.; Lee, S. Y.; Kim, J. M.; Kim, K. S.; Ahn, J. H.; Kim, P.; Choi, J. Y.; Hong, B. H. Large-scale pattern growth of graphene films for stretchable transparent electrodes. *Nature*. **2009**, *457*, 706–710.
- [28] Lin, Y. M. et al. Wafer-Scale Graphene Integrated Circuit. *Science*. **2021**, *332*, 1294–1297.
- [29] Chen M., Chang L., Zhang A. Heat-Dissipating Mobile Antenna: A Novel Mobile Antenna Concept with Extremely Small Clearance and Integrated Heat-Dissipating Function. *IEEE Trans. Antennas Propag.* **2024**, *10*, 7480–7492.
- [30] Li, H. Y.; Xiao, S. N.; Yu, H. L.; Xue, Y. H.; Yang, J. H. A review of graphene-based films for heat dissipation. *New Carbon Mater* **2021**, *36*, 897–908.
- [31] Peng, L.; Xu, Z.; Liu, Z.; Guo, Y.; Li, P.; Gao, C. Ultrahigh Thermal Conductive yet Superflexible Graphene Films. *Adv. Mater.* **2017**, *29*, 1700589.
- [32] Dong, W.; Qiu, Y.; Zhou, X.; Banas, A.; Banas, K.; Breese, M. B. H.; Cao, T.; Simpson, R. E. Tunable Mid-Infrared Phase-Change Metasurface. *Adv. Opt. Mater.* **2018**, *6*, 1701346.
- [33] Li, Y.; Abbosh, A. Reconfigurable reflectarray antenna using single-layer radiator controlled by PIN diodes. *IET Microw. Antennas Propag.* **2015**, *9*, 664–671.
- [34] Grady, N. K.; Heyes, J. E.; Chowdhury, D. R.; Zeng, Y.; Reiten, M. T.; Azad, A. K.; Taylor, A. J.; Dalvit, D. A. R.; Chen, H. T. Terahertz Metamaterials for Linear Polarization Conversion and Anomalous Refraction. *Science*. **2013**, *340*, 1304–1307.
- [35] Huang, J. X.; Fu, T.; Li, H. O.; Shou, Z. Y.; Gao, X. A reconfigurable terahertz polarization converter based on metal-graphene hybrid metasurface. *Chin. Opt. Lett.* **2020**, *18*, 013102.
- [36] Zhang, H. H.; Chao, J. B.; Wang, Y. W.; Liu, Y.; Xu, Y. X.; Yao, H. Electromagnetic-Thermal Co-Design of Base Station Antennas With All-Metal EBG Structures. *IEEE Antenn. Wirel. Pr.* **2023**, *22*, 3008–3012.
- [37] Tan, X.; Liu, T. H.; Zhou, W. J.; Yuan, Q. L.; Ying, J. F.; Yan, Q. W.; Lv, L.; Chen, L.; Wang, X. Z.; Du, S. Y.; Wan, Y. J.; Sun, R.; Nishimura, K.; Yu, J. H.; Jiang, N.; Dai, W.; Lin, C. T. Enhanced Electromagnetic Shielding and Thermal Conductive Properties of Polyolefin Composites with a Ti3C2Tx MXene/Graphene Framework Connected by a Hydrogen-Bonded Interface. *ACS Nano*. **2022**, *16*, 9254–9266.
- [38] Sun S., Jiang W., Gong S., and Hong T. Reconfigurable linear-to-linear polarization conversion metasurface based on PIN diodes. *IEEE Antenn. Wirel. Pr.* **2018**, *17*, 1722–1726.
- [39] Z. Yang et al. Reconfigurable multifunction polarization converter integrated with PIN diode. *IEEE Antennas Wireless Propag. Lett.* **2021**, *31*, 557–560.
- [40] Liu W., Ke J., Xiao C., Zhang L., Cheng Q., and Cui T. Broadband polarization-reconfigurable converter using active metasurfaces. *IEEE Trans. Antennas Propag.* **2023**, *71(4)* 3725–3730.
- [41] S. Pramanik, S. C. Bakshi, C. Koley, D. Mitra, A. Monti, and F. Bilotti. Active metasurface-based reconfigurable polarization converter with multiple and simultaneous functionalities. *IEEE Antenn. Wirel. Pr.* **2023**, *20*, 522–526.

Just Accepted

Just Accepted

Electronic Supplementary Material

Graphene-based integrated radiation heat-dissipation reconfigurable polarization conversion metasurface

Bei Dong^{1,§}, Haoran Zu^{1,§}, Rongguo Song^{1,2}(✉), Zhi Luo¹, Wei Qian¹, Ying Huang², Jingwei Zhang¹, Qinglei Du³ (✉) and Daping He¹

¹ Hubei Engineering Research Center of RF-Microwave Technology and Application, Wuhan University of Technology, Wuhan 430070, China

² Qianyan National laboratory, Hangzhou 310024, China

³ Air Force Early Warning Academy, Wuhan 430019, China

[§] Bei Dong and Haoran Zu contributed equally to this work.

Supporting information to <https://doi.org/10.26599/NR.2025.94907494>

Just Accepted

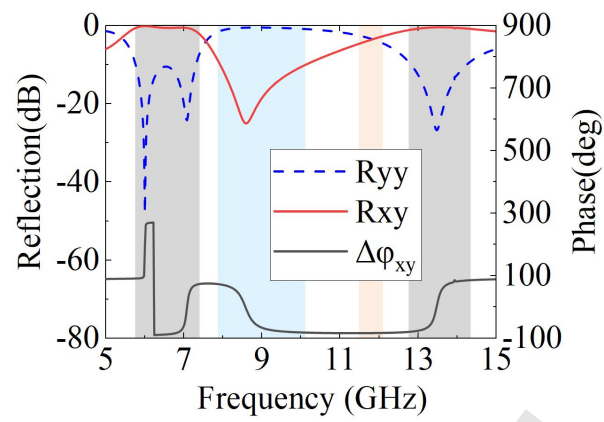


Figure S1. Simulated reflection magnitudes and phase difference when the PIN diode is reverse biased for an incident linear polarization wave oriented at $\varphi + 90^\circ$ ($\varphi = 45^\circ$) relative to the x-axis.

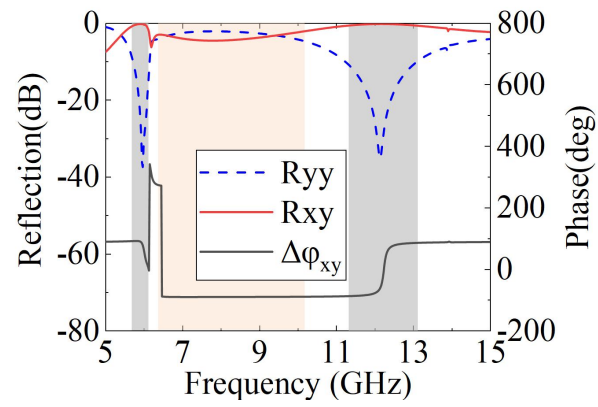


Figure S2 Simulated reflection magnitudes and phase difference when the PIN diode is forward biased for an incident linear polarization wave oriented at $\varphi + 90^\circ$ ($\varphi = 45^\circ$) relative to the x-axis.

Just Accepted

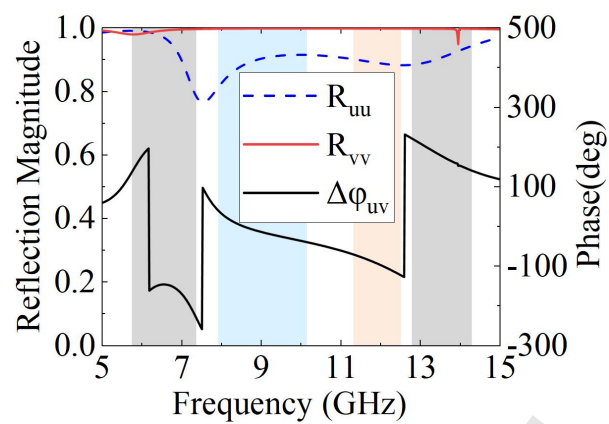


Figure S3 The reflection amplitudes and phase differences of the u and v polarization incident waves when the PIN diode is reverse biased.

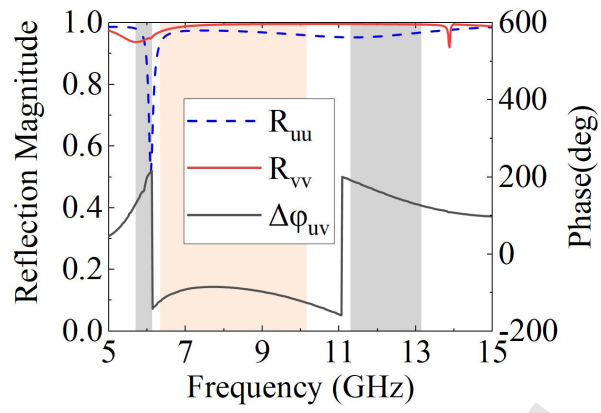


Figure S4 The reflection amplitudes and phase differences of the u and v polarization incident waves when the PIN diode is forward biased.

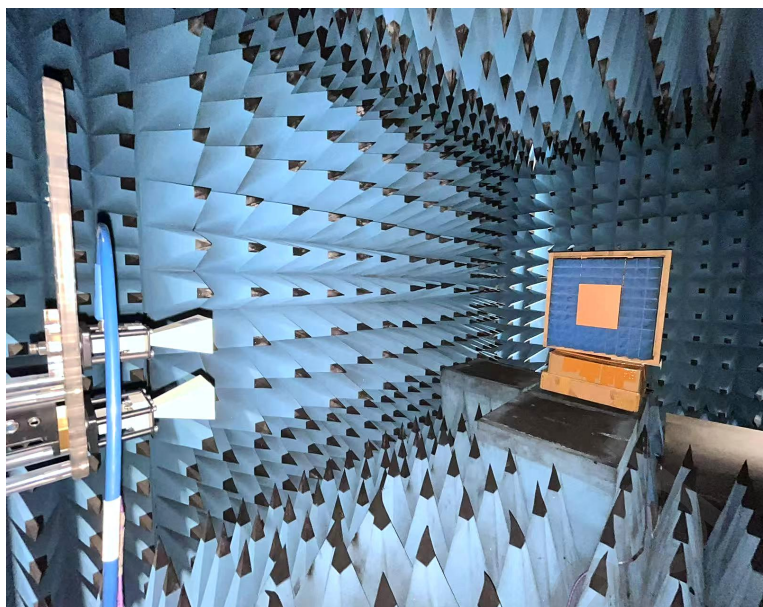


Figure S5 Copper-based Microwave Anechoic Chamber Testing System.

Just Accepted